

1 **Production of nanoparticles during experimental deformation of smectite and**
2 **implications for seismic slip**

3 **S. Aretusini¹, S. Mitterpergher², O. Plümper³, E. Spagnuolo⁴, A. F. Gualtieri⁵ and G. Di**
4 **Toro^{1,4,6}**

5

6 ¹School of Earth and Environmental Sciences, University of Manchester, Manchester, UK

7 ²Dipartimento di Scienze della Terra, Università degli Studi di Torino, Torino, Italy

8 ³Department of Earth Sciences, Utrecht University, Utrecht, The Netherlands

9 ⁴Sezione di Tettonofisica e Sismologia, Istituto Nazionale di Geofisica e Vulcanologia, Roma, Italy

10 ⁵Dipartimento di Scienze Chimiche e Geologiche, Università degli Studi di Modena e Reggio

11 Emilia, Modena, Italy

12 ⁶Dipartimento di Geoscienze, Università degli Studi di Padova, Padova, Italy.

13

14 Corresponding author: Stefano Aretusini[†] (stefano.aretusini@postgrad.manchester.ac.uk)

15 [†] School of Earth, Atmospheric and Environmental Sciences, The University of Manchester,

16 Williamson Building, Oxford Road, Manchester M13 9PL, UK.

17

18 **Highlights**

- 19 • Nanoparticles are common constituents of seismogenic fault zones
- 20 • Smectite nanoparticles are produced by mechanical amorphization during slip
- 21 • The largest production of nanoparticles occurs at intermediate slip rates (0.0003-0.1 ms⁻¹)
- 22 • Only when sheared at seismic slip rates (~1 ms⁻¹) nanoparticles promote fault weakening

23

24 **Abstract**

25 Nanoparticles and amorphous materials are common constituents of the shallow sections of
26 active faults. Understanding the conditions at which nanoparticles are produced and their
27 frictional properties can further improve our understanding of fault mechanics and earthquake
28 energy budgets. Here we present the results of 59 rotary shear experiments conducted at room-
29 dry (20-45% relative humidity) on gouge mixtures of smectite (Ca-montmorillonite, Ca-mnt) and
30 quartz. The mixtures having 60, 50, 25, 0 wt.% Ca-mnt, are analogues to natural fault gouges
31 with variable clay content. All experiments were performed at a normal stress of 5 MPa, slip rate
32 of $0.0003 \leq V \leq 1.5 \text{ ms}^{-1}$ and displacement of 3 m. To monitor the development of fabric and the
33 mineralogical changes during the experiments, we investigated the deformed gouges using
34 advanced electron microscopy combined with X-ray powder diffraction quantitative phase
35 analysis. This integrated analytical approach reveals that, at all slip rates and compositions, the
36 nanoparticles (grain size of 10-50 nm) are partly amorphous and result from cataclasis, wear and
37 mechanical solid state amorphization of smectite. The maximum production of amorphous
38 nanoparticle occurs in the intermediate slip rate range ($0.0003 \text{ ms}^{-1} \leq V \leq 0.1 \text{ ms}^{-1}$), at the highest
39 frictional work and is associated to diffuse deformation and slip strengthening behavior. Instead,
40 the lowest production of amorphous nanoparticles occurs at co-seismic slip rates ($V \geq 1.3 \text{ ms}^{-1}$), at
41 the highest frictional power and is associated to strain and heat localization and slip weakening
42 behavior. Despite the experiments presented here were conducted at room humidity conditions,
43 they suggest that, independently of the amount of smectite nanoparticles, fault weakening in
44 nature occurs only when typical seismic slip rates ($> 0.1 \text{ ms}^{-1}$) are achieved and that estimates of
45 the fracture surface energy dissipated during earthquakes might be extremely difficult to
46 constrain.

47
48 **Keywords:** smectite, earthquakes, friction, nanoparticles, clay amorphization

49 **1. Introduction**

50 Amorphous and crystalline nanoparticles are common constituents of the shallow sections of
51 natural faults [*Chester et al.*, 2005; *Ma et al.*, 2006]. As a consequence, a general issue in fault
52 mechanics is how nanoparticles form and what role they have in the seismic cycle [*Sammis and*
53 *Ben-Zion*, 2008]. For instance, the presence of nanoparticles can favor the activation of grain size-
54 dependent deformation processes [*De Paola et al.*, 2015] and the reaction kinetics at both seismic
55 and sub-seismic slip rates [*Hirono et al.*, 2013]. Moreover, the reduction in grain size of fault
56 materials during seismic rupture propagation and slip affects the earthquake energy budget [*Chester*
57 *et al.*, 2005; *Reches and Dewers*, 2005; *Ma et al.*, 2006]. Production of nanoparticles increases
58 some energy sinks (e.g., the breakdown work or the energy dissipated during rupture propagation,
59 [*Tinti et al.*, 2005]) at the expenses, for instance, of the seismic radiated energy [*Kanamori and*
60 *Rivera*, 2006]. Here, given the abundance of smectite-rich gouges in natural faults, we focus on the
61 investigation of the deformation conditions that lead to the production of nanoparticles in these
62 materials.

63 Smectite minerals, i.e. hydrous aluminum phyllosilicates, are common gouge constituents in
64 shallow fault zones, and are among the major components of fault cores sampled during the
65 scientific drilling of several seismogenic faults (e.g., [*Ohtani et al.*, 2000; *Kuo et al.*, 2009;
66 *Schleicher et al.*, 2010; *Holdsworth et al.*, 2011; *Chester et al.*, 2013]). Detailed microstructural
67 studies on gouge samples from scientific drilling in the Nojima fault [*Janssen et al.*, 2013], the San
68 Andreas fault [*Janssen et al.*, 2010] and the Chelungpu fault [*Kuo et al.*, 2009; *Janssen et al.*, 2014]
69 reported amorphous and nanocrystalline materials associated with smectite-rich fault rocks. These
70 materials included glass, amorphous rims around quartz grains and partly/fully amorphous
71 nanoparticles, often associated with recrystallized smectite minerals [*Kuo et al.*, 2009; *Schleicher et*
72 *al.*, 2010; *Janssen et al.*, 2013]. Amorphous materials and nanoparticles have also been described in
73 exhumed fault rocks, formed at expenses of granite [*Ozawa and Takizawa*, 2007] and graphite-rich
74 gouges [*Nakamura et al.*, 2015]. In general, understanding the processes and conditions that lead to

75 nanoparticles and amorphous materials production in fault rocks, will help to interpret the chemical
76 and physical processes active during the seismic cycle at shallow depths.

77 The production of nanoparticles can occur by cataclasis, wear and mechanical solid state
78 amorphization, which can reduce initial grain size down to less than 100 nm and introduce lattice
79 defects in the crystals (e.g., [Yund *et al.*, 1990; Hadizadeh *et al.*, 2015]). During and immediately
80 after seismic slip, because of the temperature increase in the slipping zone due to frictional heating
81 and subsequent cooling, diffusional processes may facilitate the recovery of lattice defects and
82 decrease the degree of amorphization [De Castro and Mitchell, 2002].

83 The effect of nanoparticles on bulk friction has been explored mainly for granitoid and
84 carbonatic rocks and gouges. The extremely small size and high specific surface area of
85 nanoparticles may promote flash melting and grain-size dependent deformation processes (i.e.
86 superplastic behavior [Ashby and Verrall, 1973]), resulting in fault weakening at seismic slip rates
87 (~ 1 m/s) and rate-weakening behavior at sub-seismic slip rates [Verberne *et al.*, 2014]. However,
88 despite nanoparticles production and its effect on bulk friction at seismic slip rates in clay-rich
89 gouges remain poorly understood, they have not been systematically studied yet [Remitti *et al.*,
90 2015].

91 Here we quantify the production of nanoparticles in smectite-bearing gouges and their
92 effects on friction combining rotary shear experiments with a systematic mineralogical and
93 microstructural characterization of the experimental products. The experiments were conducted at
94 slip rates of 0.0003 to 1.5 ms⁻¹, displacement of 3 m, and 5 MPa of normal stress, on room-dry (20-
95 45% relative humidity) gouges composed of quartz, opal and 0 to 60 wt.% smectite (Ca-
96 montmorillonite). Nanoparticles are produced in all the sheared smectite-bearing gouges with the
97 largest abundance measured at intermediate slip rates ($0.0003 \leq V \leq 0.1$ ms⁻¹). The production of
98 nanoparticles results from cataclasis, wear and mechanical amorphization of smectite. The effect of
99 nanoparticles production on bulk friction is slip strengthening at intermediate slip rates and slip
100 weakening at co-seismic slip rates. Despite the experimental results presented here were obtained

under room humidity conditions, they imply that robust estimates of energy partitioning during earthquakes may be challenging to achieve. Moreover, the presence of nanoparticles may allow the more efficient activation of thermo-chemical pressurization and of grain size-dependent processes that, together with thermal pressurization of pore fluids, will contribute to the coseismic weakening of natural faults.

2. Methods

2.1 Starting material

Since variable proportions of smectite and quartz occur in fault cores of plate boundary faults (e.g. [Kameda *et al.*, 2015]), we used four different compositions to control the effect of smectite content on nanoparticles production. We tested four materials including (i) STx-1b source clay with 60 wt.% Ca-Montmorillonite (Ca-mnt), 20 wt.% opal-CT (opal) and 20 wt.% amorphous material, purchased from Clay Minerals Society (see Section 3.2 and Table 1 for their mineral composition) [Chipera and Bish, 2001], (ii) pure crystalline quartz powder, commercially known as “micronized quartz”, (iii) 80:20 weight proportions of STx-1b and micronized quartz to obtain 50 wt.% Ca-mnt-rich gouges, and (iv) 40:60 weight proportions of STx-1b and micronized quartz to obtain 25 wt.% Ca-mnt-rich gouges. Before each experiment, the starting materials were equilibrated at room-dry conditions (20-45% relative humidity).

Scanning electron microscope (SEM) investigations conducted on 60 wt.% Ca-mnt showed that the gouge had a granular appearance, with grain sizes of $<100\ \mu\text{m}$ (Supplementary Figure 1). The individual grains consisted of micrometer-sized Ca-mnt with a fibrous-like appearance, wrapping opal grains (grain size $< 5\ \mu\text{m}$). Because of their intimate association, we could not separate the Ca-mnt grains from the opal ones. The micronized quartz powder had an initial grain size of $<100\ \mu\text{m}$.

124 2.2 Rotary shear experiments

125 Rotary shear apparatuses are currently the only experimental equipment imposing
126 deformation conditions at seismic slip rates ($0.0001 \leq V \leq 10 \text{ ms}^{-1}$) for displacements ($> 0.3 \text{ m}$) typical
127 of moderate to large in size earthquakes. To ensure reproducibility of the experiments we used two
128 different rotary shear apparatuses.

129 We performed 47 experiments using the vertical configuration rotary shear apparatus ROSA
130 (Rotary Shear Apparatus, model MIS-233-1-77 from MARUI & CO., LTD [*Rempe et al.*, 2014]),
131 installed at the Dipartimento di Geoscienze of the University of Padova (Padua, Italy). Additional
132 12 experiments were performed with the horizontal configuration rotary shear apparatus SHIVA
133 (Slow to High Velocity Apparatus [*Di Toro et al.*, 2010]), installed at the HP-HT laboratory of the
134 Istituto Nazionale di Geofisica e Vulcanologia (Rome, Italy). All experiments and their run
135 conditions are listed in Supplementary Table 1. The sample assemblages for ROSA (HCR) and
136 SHIVA (HCS) rotary apparatuses are described in Figure 1a.

137 The gouges were sheared for 3 m of equivalent displacement under a normal stress of 5 MPa
138 (for definition of equivalent displacement, velocity, etc. see [*Di Toro et al.*, 2010]). Hereafter,
139 equivalent velocity and equivalent displacement will be referred to as slip rate and displacement,
140 respectively. In ROSA, experiments with 60, 50 and 25 wt.% Ca-mnt were performed at slip rates
141 of 0.0003, 0.001, 0.01, 0.1, 0.3, 1.3, 1.5 ms^{-1} , while experiments with pure quartz powders were
142 performed at slip rates of 0.01, 0.1, 1.3 ms^{-1} (see Supplementary Table 1). In SHIVA, all
143 experiments were performed at slip rates of 0.01, 0.1 and 1.3 ms^{-1} (see Supplementary Table 1). In
144 all experiments, the gouge layer thickness w was determined as $w = |z - z_0|$, with z_0 the axial position
145 measured with no gouge in the sample holder and z the axial position during the experiment. The
146 initial gouge layer thickness w_0 was measured after compacting the gouge layer at 5 MPa normal
147 stress, before the onset of shear. All experiments had an initial gouge layer thickness $w_0 = 2 \pm 0.15$
148 mm prior to deformation. The thickness w during the experiment was divided by w_0 (normalized
149 thickness = w/w_0) to compare axial shortening data from experiments with slightly different initial

150 thickness (Figures 2d-f). The ratio of measured shear and normal stresses is defined as the friction
151 coefficient μ . The spurious friction contribution due to the sample assemblage to the total measured
152 friction coefficient and the differences in the mechanical data between ROSA and SHIVA
153 experiments are discussed in Supplementary Material 3.

154 **2.3 X-ray powder diffraction quantitative phase analyses**

155 X-ray powder diffraction (XRPD) with internal standard measurement and subsequent
156 Rietveld refinement of the diffractograms allowed us to quantify the effect of shear deformation on
157 the mineral assemblage and on the amount of amorphous material.

158 XRPD data were collected for 25, 50, 60 wt.% Ca-mnt, on both the starting and deformed
159 materials retrieved from the experiments performed with ROSA (Table 1). We analyzed the entire
160 gouge layer to avoid compositional variability due to incomplete sampling. Before each
161 measurement, ca. 10 wt.% of alumina internal standard (NIST 676A) was added to the samples.

162 Data were collected with a θ/θ diffractometer (PANalytical X'Pert Pro) equipped with a fast,
163 real time multiple step detector, and CuK α radiation (40 kV and 40 mA). To secure a random
164 smectite orientation and thus avoid grain orientation bias, sample powders were mounted on a silica
165 glass holder using the side loading technique. We used the following instrumental conditions: 3-
166 80 °2 θ range, virtual step scan of 0.0167 °2 θ and virtual time per step of 50 s. The incident beam
167 pathway included: 0.125° divergence slit, 0.125° anti-scattering slit, 0.02 rad soller slits and a 10-
168 mm copper mask. The pathway of the diffracted beam included a Ni filter, soller slits (0.02 rad) and
169 an antiscatter blade (5 mm).

170 Quantitative phase analysis (i.e., determination of both crystalline and amorphous weight
171 content) was performed using the combined Rietveld and refined intensity ratio methods [Gualtieri,
172 2000]. Rietveld data analysis was performed using the Profex-BGMN software [Bergmann *et al.*,
173 1998], which allowed us to simulate the contribution of the instrument to the broadening of the
174 Bragg's peaks and to implement complex structural models required by smectite and opal-CT
175 mineralogy (i.e. smectite turbostratic disorder and opal cristobalite-tridymite interlayering).

176 Structural models of the minerals recognized in the gouge were taken from the BGMN library for
177 quartz and for the alumina internal standard (NIST 676a) [Bergmann *et al.*, 1998]. For Ca-mnt, we
178 used the structural model comprising the turbostratic disorder [Ufer *et al.*, 2004], and for opal-CT
179 we used a supercell model simulating the irregular cristobalite-tridymite interlayering (R. Kleeberg,
180 personal communication). Refinement was limited to the 12-60° 2 θ interval to exclude the 001 peak
181 of Ca-mnt from the refinement. The Ca-mnt 001 peak intensity is sensitive to preferred orientation,
182 and its position to humidity in the measuring chamber. In general, the use of models accounting for
183 Ca-mnt turbostratic disorder and opal-CT interlayered structure strongly improved the accuracy of
184 the refinement.

185 With the Rietveld method, the accuracy of the estimation of amorphous material content
186 depends on: (i) the actual amount of amorphous material, (ii) the amount of internal standard added
187 prior to the XRPD measurements and (iii) the error of Rietveld refinement model [Westphal *et al.*,
188 2009]. In the analysis presented in this study, the actual amount of amorphous material varied
189 between ± 6.7 -10.1 wt.% with respect to the estimated content (Table 1, error bars in Figure 4). Such
190 variation was calculated considering: (i) 10 wt.% of internal standard, (ii) 1% of Rietveld error and
191 (iii) actual amount of amorphous material of 25, 10 and 5 wt.% (for 60, 50 and 25 wt.% Ca-mnt,
192 respectively).

193 **2.4 Microstructural analysis**

194 Starting material and deformed gouge layers were (i) embedded within epoxy resin
195 (Araldite2020®, Epofix), (ii) cut perpendicular to the slip surface (radial or tangential sections,
196 Figure 1b) and (iii) polished in dry conditions for SEM investigations. Twenty-four gouge layers
197 (ROSA experiments) were cut and polished along a tangential section (Figures 1a-b). The polished
198 blocks were investigated using backscattered electron (BSE) imaging within a CamScan
199 MX3000 SEM (University of Padova).

200 Four additional samples with 60 wt.% Ca-mnt (starting and sheared materials at $V=0.01$, 0.1
201 and 1.5 ms⁻¹) deformed with SHIVA were cut and polished along a radial section (Figure 1b).

202 Ultrathin, electron-transparent lamellae (100-150 nm thick), were prepared using a FEI Helios
203 Nanolab FIB-SEM (Utrecht University). The FIB-SEM lamellae were oriented parallel to the slip
204 vector (Figure 1c). The FIB-SEM lamellae were analyzed in FEI Tecnai and FEI Talos transmission
205 electron microscopes (TEM) (Utrecht University), using bright field (BF) and high angle annular
206 dark field (HAADF) imaging as well as selected area electron diffraction (SAED) and energy
207 dispersive X-ray spectroscopy (EDS).

208 **3. Results**

209 **3.1 Rotary shear experiments**

210 **3.1.1 Evolution of the friction coefficient with displacement**

211 We obtained reproducible mechanical data using ROSA and SHIVA at identical imposed
212 deformation conditions (see discussion in the Supplementary Material 2).

213 Experiments performed at $V=0.01 \text{ ms}^{-1}$ were representative of the mechanical data in the
214 $0.0003\text{-}0.01 \text{ ms}^{-1}$ slip rate range (Figure 2a, Supplementary Table 1). Friction coefficient μ in pure
215 quartz gouges decreased with displacement (slip-weakening behavior), whereas μ in Ca-mnt
216 bearing gouges increased with displacement (slip-strengthening behavior), after a short weakening
217 phase in the first $\sim 0.1 \text{ m}$ of slip (Figure 2a). A second peak of friction coefficient and a subsequent,
218 reproducible, friction drop occurred after ca. 0.75 m of displacement on 50 wt.% Ca-mnt gouges
219 (arrow in Figure 2a; Supplementary Material 2).

220 Experiments performed at $V=0.1 \text{ ms}^{-1}$ were representative of the mechanical data in the 0.1-
221 0.3 ms^{-1} slip rate range (Figure 2b). Pure quartz gouge was slip-strengthening in the first $\sim 0.4 \text{ m}$ of
222 displacement, after which it attained a monotonic slip-weakening behavior. Instead, gouges with
223 Ca-mnt had an initial peak friction coefficient followed by slip-weakening and, after ca. 0.1 m of
224 displacement, by slow and monotonic slip-strengthening until slip ceased. In general, slip-
225 strengthening was less pronounced compared to the experiments performed at $0.0003 \leq V \leq 0.01$

ms⁻¹. The 50 wt.% Ca-mnt gouge had a second peak in μ after ~1 m of displacement and a subsequent drop in friction (arrow in Figure 2b).

Experiments performed at $V=1.3$ ms⁻¹ were characterized by the approx. exponential decay of μ as was observed in experiments performed by [Mizoguchi *et al.*, 2007]. Similar to the experiments performed at lower slip rates, quartz gouges had a short (< 0.3 m) slip-strengthening behavior before μ decreased monotonically with displacement (Figure 2c). In contrast, all Ca-mnt-bearing gouges had a similar initial rapid decay of μ towards a minimum that decreased with increasing Ca-mnt content (Figure 2c). For 50 and 60 wt.% Ca-mnt, after an initial monotonic slip weakening, the frictional behavior was irregular, with the occurrence of a second peak in friction between 1 and 2 meters of displacement (stars in Figure 2c).

3.1.2 Evolution of gouge thickness with displacement

Pure quartz gouges compacted at all imposed slip rates. In particular, large compaction at the onset of displacement was concomitant with slip-strengthening and followed by reduced to negligible compaction associated to monotonic slip-weakening until the end of the experiment (Figures 2d-f). For all Ca-mnt gouge mixtures and independently of the imposed slip rate, compaction was concomitant with slip-weakening at the onset of displacement. With increasing slip and at all slip rates, initial compaction was followed, by pronounced dilatancy for 60 wt.% Ca-mnt gouge mixtures, negligible dilatancy for 50 wt.% Ca-mnt mixtures and further compaction for 25 wt.% Ca-mnt mixtures (Figures 2d-f). In our experiments, extrusion of powders from the sample holder occurred in the 25 and 50 wt.% Ca-mnt mixtures sheared at $V=0.01$ ms⁻¹ for displacements larger than ca. 1.5 m (large w/w_0 decrease indicated by the arrow in Figure 2d).

3.1.3 Evolution of friction coefficient with slip rate

To compare the friction coefficient values of all experiments, we calculated $\mu_{2.75}$ as the averaged friction coefficient at 2.75 ± 0.025 m of displacement (Figure 3, Supplementary Table 1). Any variation of $\mu_{2.75}$ with slip rate is described here as either rate-weakening (friction coefficient

251 decreases with slip rate) or rate-strengthening (friction coefficient increases with slip rate) but not in
252 terms of the rate and state friction law [Dieterich, 1979]. In pure quartz gouges, $\mu_{2.75}$ was rate-
253 weakening. Instead, in Ca-mnt gouges $\mu_{2.75}$ evolved from rate-strengthening to rate-weakening with
254 increasing slip rate. The slip rate at which the frictional behavior changed was composition-
255 dependent: $V=0.01 \text{ ms}^{-1}$ in 60 wt.% and $V=0.001 \text{ ms}^{-1}$ in 50 and 25 wt.% Ca-mnt.

256 3.2 Quantitative phase analysis and the amount of amorphous material

257 The weight fraction of the amorphous material (Section 2.3) increased with respect to its
258 initial concentration in all the sheared Ca-mnt gouges. However, for the gouge with a 25 wt.% Ca-
259 mnt mixtures, the increase was below the detection limit (Figure 4, Table 1). The increase or
260 production of amorphous material was associated to the decrease of Ca-mnt abundance and was
261 higher in the experiments performed at low slip rates. Instead, the opal and quartz content was the
262 same as the starting material across all the tested slip rates. The quantitative phase analysis suggests
263 that the production of amorphous material occurred at the expense of Ca-mnt at all slip rates and
264 that it was more efficient at $V \leq 0.1 \text{ ms}^{-1}$.

265 3.3 Microstructures

266 Following previous investigations conducted on clay-rich gouges deformed with rotary
267 shear machines [Kitajima *et al.*, 2010; French *et al.*, 2014], we describe below the microstructures
268 found in our experiments by defining four types of microstructural domains distinguished by grain
269 size and by the presence of clay clast aggregates (CCAs) and micro-foliations [Boutareaud *et al.*,
270 2008; Ferri *et al.*, 2011] (Figures 5-6). The occurrence of the four domains in the deformed gouges
271 as a function of the initial Ca-mnt content and of the imposed slip rate is reported in Figures 7-8.

272 **Domain U (Undeformed)** has angular quartz clasts and sub-rounded aggregates of opal and
273 Ca-mnt, with a relative abundance depending on the starting composition (Figure 5a). At the nano-
274 scale, the Ca-mnt is interlayered with opal (Figures 6a-b). Selected area electron diffraction (SAED)
275 of Ca-mnt crystals showed a pattern with diffraction rings, implying a partially crystalline to

276 crystalline structure (inset in Figure 6a). Domain U is identical to the undeformed starting material
277 (Supplementary Figure 1).

278 **Domain LS (Low Strain)** has sub-rounded opal and quartz clasts, with grain size smaller
279 than in domain U. In gouges with Ca-mnt ≥ 50 wt.%, clasts are surrounded by a Ca-mnt-rich matrix
280 and form CCAs with Ca-mnt cortex wrapping opal or quartz nuclei (Figure 5b). In gouges with 25
281 wt.% Ca-Mnt, CCAs are absent and matrix is more quartz-rich.

282 **Domain HSf (High Strain foliated)** is organized in two subdomains: A and B (Figure 5c).
283 Both subdomains include individual nanoparticles, clusters of nanoparticles, nanocrystals and
284 CCAs with opal or quartz core and nanoparticles cortex (Figures 6c-e). Subdomain A has a foliated
285 texture, sub-micrometric grain size and few CCAs. Subdomain B has a granular texture with
286 abundant CCAs. The widespread presence of CCAs in B suggests lower shear strain compared to A
287 (see [Rempe *et al.*, 2014] for a discussion). In subdomains A and B, SAED patterns show both
288 diffuse scattering and diffraction rings, due to the coexistence of amorphous nanoparticles and Ca-
289 mnt nanocrystals (subset in Figure 6d). Based on EDS-TEM element mapping, nanoparticles
290 contain Al and Si suggesting a smectitic composition (Figure 6f).

291 **Domain HS (High Strain)** is similar to subdomain HSf-A (i.e., presence of nanoparticles,
292 Ca-mnt crystals and CCAs), but is not foliated (Figures 5d and 6g-h). Ca-mnt crystals have periodic
293 lattice spacing and are ubiquitous (Figure 6h). With increasing initial quartz content ($> 40\%$ in wt.),
294 the domain HS is enriched in micrometric in size sub-rounded quartz grains and is systematically
295 cut or bounded by Y-shears (e.g., [Logan *et al.*, 1992]) (Figures 5e-f).

296 In general, independently of the initial gouge composition and of the imposed slip rate, high
297 strain domains (HSf, HS) sharply crosscut the low strain (LS) or undeformed (U) domains (Figure
298 7). The association of domain LS with HSf was found in the gouges sheared at the lowest slip rates,
299 which were also the gouges that recorded diffuse deformation (Figure 7) and the largest production
300 of amorphous material (i.e. amorphous material measured after the experiment minus amorphous
301 material in the starting material, Figure 8). Instead, the association of domains U or LS with HS was

302 found in the gouges sheared at seismic slip rates, which were also the gouges that recorded
303 localized deformation, represented by Y-shears in HS (Figure 7), and the lowest amorphous
304 production (Figure 8).

305 **4. Discussion**

306 **4.1 The amorphous nature of smectite nanoparticles**

307 The XRPD quantitative phase analysis of the sheared gouges show that, comparing
308 deformed gouges (independently of the imposed slip rate) with the starting material, the amorphous
309 material content increases and Ca-mnt content decreases, while the quantities of all the other phases
310 remain constant (Figure 4, Section 3.2). Consequently, Ca-mnt is the source for the produced
311 amorphous material. Additionally, amorphous material is increased in the sheared gouges compared
312 to undeformed ones, indicating a net production of amorphous material. The production of
313 amorphous material represents a bulk increase of lattice disorder (i.e. decreased scattering power
314 under X-rays) of Ca-mnt grains due to the formation of lattice defects within the grains and the
315 increase of grain boundaries due to reduced grain size.

316 SEM imaging showed that high strain domains (HS and HSf) had an average grain size
317 below 1 μm (Figures 5c to 5f). In gouges with 60 wt.% Ca-Mnt, TEM imaging revealed that
318 nanoparticles were abundant in the high strain domains (Figures 6c-d). SAED and TEM imaging
319 showed that nanoparticles were either predominantly amorphous (domain HSf, Figure 6d) or
320 crystalline (domain HS, Figure 6h). We conclude that the amorphous material measured with XRD
321 in the bulk gouge is representative of the abundance of nanoparticles (both amorphous and
322 crystalline). However, amorphous material production may be higher when associated with
323 amorphous nanoparticles in domain HSf, due to the combination of domain thickness (Figure 9a)
324 and increased amorphization degree of the single nanoparticles (Figure 6).

325 4.2 Formation of nanoparticles and mechanical properties

326 In gouges with 50 and 60 wt.% Ca-mnt, the thickness of the domain HSf and thus the
327 content of amorphous nanoparticles varies with slip rate (Figure 9a): amorphous nanoparticles are
328 more abundant when associated to slip strengthening ($V \leq 0.1 \text{ ms}^{-1}$), and less abundant when
329 associated to slip neutral ($0.1 \leq V \leq 0.3 \text{ ms}^{-1}$) or weakening ($V \geq 1.3 \text{ ms}^{-1}$) behavior, respectively
330 (Figure 2).

331 The slip strengthening behavior results in work hardening which induces cataclasis, wear
332 and mechanical amorphization. Nanoparticles have a high strength as their grain size is close to the
333 minimum one attainable by fracturing and wear processes [*Sammis and Ben-Zion, 2008*]. If
334 nanoparticles reach the minimum grain size by fracturing, further deformation is accommodated by
335 plastic processes (i.e. dislocation glide at low temperatures or high slip rates), possibly leading to
336 accumulation of lattice defects and therefore to solid state amorphization. During deformation, if
337 nanoparticles have high strength, shear deformation may transfer (strain delocalization) to the
338 coarser and weaker low strain (LS) domain. During the experiment this process could lead to the
339 thickening of amorphous nanoparticle-rich high strain foliated (HSf) domain and, possibly, to slip
340 strengthening behavior.

341 Frictional behavior evolves from slip-neutral (for $0.1 \leq V \leq 0.3 \text{ ms}^{-1}$) to slip-weakening ($V \geq 1.3$
342 ms^{-1}), with progressively more efficient strain localization in domain HS. In this domain, the larger
343 abundance of crystalline nanoparticles can be related to strain and heat localization determining
344 either a less advanced amorphization process (i.e. because, as mechanical energy is dissipated into
345 heat, less is available for amorphization) or to a more efficient recovery mechanism for lattice
346 defects that reduces the degree of amorphization of the nanoparticles. Here, a positive feedback
347 with strain localization may occur, with heat localization favoring grain size dependent deformation
348 processes, reducing nanoparticles strength and favoring further strain localization. At seismic slip
349 rates ($V \geq 1.3 \text{ ms}^{-1}$), we suggest that smectite nanoparticles have a superplastic behavior which leads
350 to frictional weakening (e.g., [*Verberne et al., 2014; Green et al., 2015*]). At the same time, we

cannot exclude that part of frictional weakening may occur as a result of Ca-mnt dehydration and consequent pore fluid (liquid or vaped water) overpressure during cataclasis and amorphization [Brantut *et al.*, 2008; Ferri *et al.*, 2011]. However, we did not identify any fluidization texture in domain HS that could be indicative of pore fluid pressurization.

In gouges with 25 wt.% Ca-mnt, the production of amorphous nanoparticles is limited, concomitant to slip strengthening ($V \leq 0.001 \text{ ms}^{-1}$) (Figure 9a) and associated to domain HSf (Figure 8c). At higher slip rates, production of amorphous nanoparticles is negligible, concomitant to slip weakening and associated to domain HS. In pure quartz gouges, slip weakening occurs at all tested slip rates ($0.01 \leq V \leq 0.3 \text{ ms}^{-1}$) and is associated to the formation of domain HS. In these smectite-poor cases, the formation of the HS domain is indicative of efficient strain localization compared to the smectite-rich gouges. Efficient strain localization limits the gouge volume affected by mechanical amorphization, and consequently induces a negligible production of amorphous material. Strain localization can be enhanced at $V \geq 0.001 \text{ m/s}$ as quartz-rich gouges showed efficient dynamic weakening due to silica gel formation [Di Toro *et al.*, 2004].

To generalize the experimental conditions at which amorphous nanoparticles are produced we introduce the frictional work density (*FWD*), representing the total work dissipated in the slipping zone and the frictional power density (*FPD*), representing the total power dissipated in the slipping zone (e.g., [Di Toro *et al.*, 2011]). These can be defined as:

$$FWD = \int_0^X \tau(x) dx \quad \text{Eq.2}$$

with X the total displacement and $\tau(x)$ the shear stress evolution with displacement x , and

$$FPD = FWD / \Delta t \quad \text{Eq. 3}$$

with Δt the duration of the experiment (Supplementary Table 1).

In the experiments discussed here, the production of amorphous nanoparticles increased with frictional work density (Figure 9b) and decreased with frictional power density (Figure 9c). The relationships between the production of amorphous material and the occurrence of microstructural domain HSf (Figures 8 and 9a), the frictional work (Figure 9b), the frictional power

377 (Figure 9c) densities and slip rates (Figure 9), suggest that the largest production of amorphous
378 nanoparticles occurred with frictional work densities larger than 10 MJ m^{-1} and frictional power
379 densities lower than 0.4 MWm^{-2} . These trends suggest that the processes of mechanical
380 amorphization are less effective with higher *FPD* and thus higher heat dissipation. This is coherent
381 with the previous studies on the production of nanoparticles by wear and subsequent solid state
382 amorphization in high energy ball milling: mechanical heat dissipation can facilitate
383 recrystallization or recovery of lattice defects [De Castro and Mitchell, 2002].
384

385 **4.3 Geological implications of nanoparticles production**

386 Nanoparticles in smectite-rich fault gouges have been found in all cores of shallow fault
387 sections when systematic nano-analysis were performed [Schleicher *et al.*, 2010; Hirono *et al.*,
388 2014; Janssen *et al.*, 2015]. In most cases, some nanoparticles were amorphous, though they could
389 have been autogenic smectites formed in the pores of the fault gouge from alteration of silicate-
390 bearing minerals or precipitated from percolating fluids [Schleicher *et al.*, 2010]. Despite the
391 experiments presented here were conducted under room-humidity conditions and under the same
392 normal stress limited to 5 MPa, the systematic analysis of the experimental fault products has the
393 following implications for the mechanics of the shallow sections of brittle faults.

394 The interpretation of the experimental data suggests that the production of nanoparticles is
395 larger at high frictional works rather than at high work rates (Fig. 9). According to Eq. 2, the
396 frictional work increases with shear stress and, thus, with effective normal stress. As a consequence,
397 at sub-seismic to almost seismic slip rates, the amount of nanoparticle production is expected to
398 increase with depth, till, at higher ambient temperatures, smectite will be replaced by more stable
399 minerals (e.g., illite). Instead, given that frictional work rate is proportional to both the effective
400 normal stress and slip rate (Eq. 3), during seismic slip the amount of nanoparticle production is
401 expected to be further reduced with respect to the experiments discussed here. In fact, the reduction
402 of the slip weakening distance and of the slip distance required for strain localization with

403 increasing normal stress [*Di Toro et al.*, 2011; *Smith et al.*, 2015]. In addition, the fast growth of
404 nanoparticles during post-seismic cooling [*Sammis and Ben-Zion*, 2008] will reduce the amount of
405 produced and survived nanoparticles in the slipping zone. In other words, given the same amount of
406 slip accommodated by the fault, most nanoparticles and amorphous materials found (and survived)
407 in natural faults are expected to be produced during aseismic creep.

408 The clast size distribution in natural slipping zones has been used to estimate the breakdown
409 work component of an earthquake energy budget [*Chester et al.*, 2005; *Ma et al.*, 2006]. The
410 relative abundance of nanoparticles is a major contributor to the measurement of the surface
411 fracture energy. In the case of the Punchbowl and Chelungpu Faults, the clast size distributions
412 allowed the authors to estimate that the formation of new grains dissipated up to 6 % of the
413 breakdown work during seismic faulting, the remnant being dissipated during sliding on fault plane
414 [*Chester et al.*, 2005; *Ma et al.*, 2006]. However, if nanoparticles in nature were mainly produced at
415 low slip rates, possibly sub-seismic, as the experimental results discussed here suggest, and those
416 formed during seismic slip may have been grown up during cooling of the slipping zone, the
417 contribution of ultra-comminution to the breakdown work might be overestimated or extremely
418 difficult to constrain.

419 The experiments also indicate that the abundance of nano-particles is not as important as the
420 slip rate in controlling the frictional behavior of the sheared smectite-rich gouges (Figures 2 and 4).
421 Though smectite-rich ($\geq 50\%$ Ca-Mnt) gouges are more velocity-weakening than smectite-poor
422 gouges ($< 50\%$ Ca-Mnt), is the slip rate that matters (Figure 3). The direct extrapolation of these
423 experimental observations to nature would imply that the formation of smectite nanoparticles may
424 induce strengthening or weakening depending on the slip rate and, to a less extent, the smectite
425 content. The slip-strengthening behavior observed during large production of nanoparticles at
426 intermediate slip rates (Figures 2 and 4) may have the following implications: at slip rates ~ 1 mm/s
427 or less (during the late stages of coseismic slip or during afterslip), slip-strengthening would induce
428 either the arrest of fault slip (if the fault core is stronger than the principal slipping zone) or the

thickening of the principal slipping zone (if fault core is weaker than nanoparticle-rich principal slipping zone. Approaching seismic slip rates, the presence of nanoparticles produced by mechanical amorphization, which have high lattice disorder and reduced activation energy for decomposition reactions, will make the release of OH- groups (and thermomechanical pressurization) more efficient [Hirono *et al.*, 2013]. Though thermal pressurization of pore fluids probably have a pivotal role in dynamic weakening of smectite-rich gouges [Veveakis *et al.*, 2007], there is no reason to exclude that, especially with progressive seismic slip, thermochemical pressurization [Brantut *et al.*, 2008; Ferri *et al.*, 2011] and possibly grain-size dependent processes [Verberne *et al.*, 2014; De Paola *et al.*, 2015; Green *et al.*, 2015; Spagnuolo *et al.*, 2015] may contribute to dynamic weakening of natural faults. By looking at Fig. 2, the larger is the abundance of nanoparticles, especially if amorphous because produced during the other stages of the seismic cycle, the faster should be the seismic dynamic weakening in natural slipping zones.

5. Conclusions

We conducted a series of rotary shear experiments on 60-40 wt.%, 50-50 wt.%, 25-75 wt.% smectite (Ca-montmorillonite, Ca-mnt) + quartz + opal mixtures and on pure quartz gouges. All experiments were performed under room-dry conditions (20-45% relative humidity) on a 2-mm thick gouge layer by imposing the same normal stress (5 MPa) and displacement (3 m), whereas slip rates ranged from 0.0003 to 1.5 ms⁻¹ (Supplementary Table 1). We analyzed the starting and the deformed materials with SEM, FIB-SEM, TEM and XRPD quantitative phase analysis to describe the microstructures, determine the mineral content and production of amorphous material depending on the experimental conditions (Figures 4-8). The main conclusions are:

- 1) Nanoparticles (Figure 6), found in high strain microstructural domains (HSf and HS; Figure 5), are produced by mechanical solid state amorphization of Ca-mnt (Figure 4). Nanoparticles are mainly amorphous in domain HSf and crystalline in domain HS (Figure 6).

- 2) Nanoparticles production and degree of amorphization changes with slip rate and composition depending on strain localization. The maximum production of amorphous nanoparticles (20 wt.%) is at intermediate slip rates ($0.0003 \leq V \leq 0.1 \text{ ms}^{-1}$), high Ca-mnt abundance ($\text{Ca-mnt} \geq 50 \text{ wt.}\%$), concomitant to strain delocalization in the gouge layer associated to slip-strengthening behavior. With decreasing smectite content, these conditions are limited to the lowermost slip rates (i.e. at $0.0003 \leq V \leq 0.01 \text{ ms}^{-1}$ with 25 wt.% Ca-mnt). In contrast, the production of crystalline nanoparticles (5-10 wt.%) occurs at co-seismic slip rates ($V \geq 1.3 \text{ ms}^{-1}$), concomitant to strain localization in the gouge layer associated to slip weakening behavior.
- 3) Amorphous nanoparticles production changes with slip rate depending on dissipation of mechanical energy. Maximum production of amorphous nanoparticles occurs with large frictional work (10 MJ m^{-1}) and low frictional power (0.4 MW m^{-2}) density.
- 4) According to the experimental evidence reported here, in smectite-rich natural faults, nanoparticles are produced by cataclasis, wear and mechanical solid state amorphization.
- 5) Despite the experiments presented here were conducted at room humidity conditions, some implications for natural faults can still be made. First, fault weakening occurs only when typical seismic slip rates ($> 0.1 \text{ ms}^{-1}$) are achieved and the amount of weakening increases with the abundance of nanoparticles and amorphous materials. Second, because nanoparticles are more abundant when produced at intermediate and possibly sub-seismic slip rates, estimates of the fracture surface energy dissipated during earthquakes might be extremely difficult to constrain.

6. Acknowledgements

Two anonymous reviewers and the Editor are acknowledged for their very constructive comments. SA, ES and GDT acknowledge the ERC Consolidator grant 614705 NOFEAR. SA thanks Leonardo Tauro for advices on sample preparation, Federico Zorzi for help with the Rietveld

478 modelling and Reinhard Kleeberg for the opal-CT structure used in Rietveld refinements and
479 helpful advices on Rietveld modelling.

480 **Reference list**

481 Ashby, M. F., and R. A. Verrall (1973), Diffusion-accommodated flow and superplasticity, *Acta*
482 *Metall.*, 21(2), 149–163, doi:10.1016/0001-6160(73)90057-6.

483 Bergmann, J., P. Friedel, and P. Kleeberg (1998), BGMN - a New Fundamental Parameters Based
484 Rietveld Program for Laboratory X-ray Sources, it's Use in Quantitative Analysis and
485 Structure Investigations, in *CPD Newsletter*, vol. 20, pp. 5–8.

486 Boutareaud, S., D.-G. Calugaru, R. Han, O. Fabbri, K. Mizoguchi, A. Tsutsumi, and T. Shimamoto
487 (2008), Clay-clast aggregates: A new textural evidence for seismic fault sliding?, *Geophys.*
488 *Res. Lett.*, 35(5), doi:10.1029/2007GL032554.

489 Brantut, N., A. Schubnel, J.-N. Rouzaud, F. Brunet, and T. Shimamoto (2008), High-velocity
490 frictional properties of a clay-bearing fault gouge and implications for earthquake
491 mechanics, *J. Geophys. Res.*, 113(B10), doi:10.1029/2007JB005551.

492 Chester, F. M. et al. (2013), Structure and Composition of the Plate-Boundary Slip Zone for the
493 2011 Tohoku-Oki Earthquake, *Science*, 342(6163), 1208–1211,
494 doi:10.1126/science.1243719.

495 Chester, J. S., F. M. Chester, and A. K. Kronenberg (2005), Fracture surface energy of the
496 Punchbowl fault, San Andreas system, *Nature*, 437(7055), 133–136,
497 doi:10.1038/nature03942.

498 Chipera, S. J., and D. L. Bish (2001), Baseline studies of the clay minerals society source clays:
499 powder X-ray diffraction analyses, *Clays Clay Miner.*, 49(5), 398–409.

500 De Castro, C., L., and B. Mitchell S. (2002), Nanoparticles from mechanical attrition, in *Synthesis,*
501 *functionalization and surface treatment of nanoparticles*, pp. 1–14.

502 De Paola, N., R. E. Holdsworth, C. Viti, C. Collettini, and R. Bullock (2015), Can grain size
 503 sensitive flow lubricate faults during the initial stages of earthquake propagation?, *Earth*
 504 *Planet. Sci. Lett.*, *431*, 48–58, doi:10.1016/j.epsl.2015.09.002.

505 Di Toro, G., D. L. Goldsby, and T. E. Tullis (2004), Friction falls towards zero in quartz rock as
 506 slip velocity approaches seismic rates, *Nature*, *427*, 436–439.

507 Di Toro, G. et al. (2010), From field geology to earthquake simulation: a new state-of-the-art tool to
 508 investigate rock friction during the seismic cycle (SHIVA), *RENDICONTI LINCEI*, *21*(S1),
 509 95–114, doi:10.1007/s12210-010-0097-x.

510 Di Toro, G., R. Han, T. Hirose, N. De Paola, S. Nielsen, K. Mizoguchi, F. Ferri, M. Cocco, and T.
 511 Shimamoto (2011), Fault lubrication during earthquakes, *Nature*, *471*(7339), 494–498,
 512 doi:10.1038/nature09838.

513 Dieterich, J. H. (1979), Modeling of rock friction: 1. Experimental results and constitutive
 514 equations, *J. Geophys. Res.*, *84*(B5), 2161–2168, doi:10.1029/JB084iB05p02161.

515 Ferri, F., G. Di Toro, T. Hirose, R. Han, H. Noda, T. Shimamoto, M. Quaresimin, and N. De Rossi
 516 (2011), Low- to high-velocity frictional properties of the clay-rich gouges from the slipping
 517 zone of the 1963 Vaiont slide, northern Italy, *J. Geophys. Res. Solid Earth*, *116*, 1–17,
 518 doi:10.1029/2011JB008338.

519 French, M. E., H. Kitajima, J. S. Chester, F. M. Chester, and T. Hirose (2014), Displacement and
 520 dynamic weakening processes in smectite-rich gouge from the Central Deforming Zone of
 521 the San Andreas Fault, *J. Geophys. Res. Solid Earth*, *119*(3), 1777–1802,
 522 doi:10.1002/2013JB010757.

523 Green, H. W., F. Shi, K. Bozhilov, G. Xia, and Z. Reches (2015), Phase transformation and
 524 nanometric flow cause extreme weakening during fault slip, *Nat. Geosci.*, *8*(6), 484–489,
 525 doi:10.1038/ngeo2436.

526 Gualtieri, A. F. (2000), Accuracy of XRPD QPA using the combined Rietveld-RIR method, *J. Appl.*
 527 *Crystallogr.*, *33*, 267–278, doi:10.1107/S002188989901643X.

528 Hadizadeh, J., T. E. Tullis, J. C. White, and A. I. Konkachbaev (2015), Shear localization, velocity
529 weakening behavior, and development of cataclastic foliation in experimental granite gouge,
530 *J. Struct. Geol.*, *71*, 86–99, doi:10.1016/j.jsg.2014.10.013.

531 Hirono, T., W. Tanikawa, G. Honda, J. Kameda, J. Fukuda, and T. Ishikawa (2013), Importance of
532 mechanochemical effects on fault slip behavior during earthquakes:
533 MECHANOCHEMICAL EFFECT DURING EARTHQUAKE, *Geophys. Res. Lett.*, *40*(12),
534 2988–2992, doi:10.1002/grl.50609.

535 Hirono, T., J. Kameda, H. Kanda, W. Tanikawa, and T. Ishikawa (2014), Mineral assemblage
536 anomalies in the slip zone of the 1999 Taiwan Chi-Chi earthquake: Ultrafine particles
537 preserved only in the latest slip zone, *Geophys. Res. Lett.*, *41*(9), 3052–3059,
538 doi:10.1002/2014GL059805.

539 Holdsworth, R. E., E. W. E. van Diggelen, C. J. Spiers, J. H. P. de Bresser, R. J. Walker, and L.
540 Bowen (2011), Fault rocks from the SAFOD core samples: Implications for weakening at
541 shallow depths along the San Andreas Fault, California, *J. Struct. Geol.*, *33*(2), 132–144,
542 doi:10.1016/j.jsg.2010.11.010.

543 Janssen, C., R. Wirth, E. Rybacki, R. Naumann, H. Kemnitz, H.-R. Wenk, and G. Dresen (2010),
544 Amorphous material in SAFOD core samples (San Andreas Fault): Evidence for crush-
545 origin pseudotachylytes?, *Geophys. Res. Lett.*, *37*(1), L01303, doi:10.1029/2009GL040993.

546 Janssen, C., R. Wirth, A. Lin, and G. Dresen (2013), TEM microstructural analysis in a fault gouge
547 sample of the Nojima Fault Zone, Japan, *Tectonophysics*, *583*, 101–104,
548 doi:10.1016/j.tecto.2012.10.020.

549 Janssen, C., R. Wirth, H.-R. Wenk, L. Morales, R. Naumann, M. Kienast, S.-R. Song, and G.
550 Dresen (2014), Faulting processes in active faults – Evidences from TCDP and SAFOD drill
551 core samples, *J. Struct. Geol.*, *65*, 100–116, doi:10.1016/j.jsg.2014.04.004.

552 Janssen, C., R. Naumann, L. Morales, R. Wirth, D. Rhede, and G. Dresen (2015), Co-seismic
 553 and/or a-seismic microstructures of JFAST 343 core samples from the Japan Trench, *Mar.*
 554 *Geol.*, *362*, 33–42, doi:10.1016/j.margeo.2015.01.013.

555 Kameda, J., M. Shimizu, K. Ujiie, T. Hirose, M. Ikari, J. Mori, K. Oohashi, and G. Kimura (2015),
 556 Pelagic smectite as an important factor in tsunamigenic slip along the Japan Trench,
 557 *Geology*, *43*(2), 155–158, doi:10.1130/G35948.1.

558 Kanamori, H., and L. Rivera (2006), Energy Partitioning During an Earthquake, in *Earthquakes:*
 559 *Radiated Energy and the Physics of Faulting*, edited by R. Abercrombie, A. McGarr, G. D.
 560 Toro, and H. Kanamori, pp. 3–13, American Geophysical Union.

561 Kitajima, H., J. S. Chester, F. M. Chester, and T. Shimamoto (2010), High-speed friction of
 562 disaggregated ultracataclasite in rotary shear: Characterization of frictional heating,
 563 mechanical behavior, and microstructure evolution, *J. Geophys. Res.*, *115*(B8),
 564 doi:10.1029/2009JB007038.

565 Kuo, L.-W., S.-R. Song, E.-C. Yeh, and H.-F. Chen (2009), Clay mineral anomalies in the fault
 566 zone of the Chelungpu Fault, Taiwan, and their implications, *Geophys. Res. Lett.*, *36*(18),
 567 doi:10.1029/2009GL039269.

568 Logan, J. M., C. A. Dengo, N. G. Higgs, and Z. Z. Wang (1992), Fabrics of experimental fault
 569 zones: their development and relationship to mechanical behavior., *Fault Mech. Transp.*
 570 *Prop. Rock*, 33–67, doi:10.1016/S0074-6142(08)62814-4.

571 Ma, K.-F. et al. (2006), Slip zone and energetics of a large earthquake from the Taiwan Chelungpu-
 572 fault Drilling Project, *Nature*, *444*(7118), 473–476, doi:10.1038/nature05253.

573 Mizoguchi, K., T. Hirose, T. Shimamoto, and E. Fukuyama (2007), Reconstruction of seismic
 574 faulting by high-velocity friction experiments: An example of the 1995 Kobe earthquake,
 575 *Geophys. Res. Lett.*, *34*(1), doi:10.1029/2006GL027931.

576 Nakamura, Y., K. Oohashi, T. Toyoshima, M. Satish-Kumar, and J. Akai (2015), Strain-induced
 577 amorphization of graphite in fault zones of the Hidaka metamorphic belt, Hokkaido, Japan,
 578 *J. Struct. Geol.*, 72, 142–161, doi:10.1016/j.jsg.2014.10.012.

579 Ohtani, T., K. Fujimoto, H. Ito, H. Tanaka, N. Tomida, and T. Higuchi (2000), Fault rocks and past
 580 to recent fluid characteristics from the borehole survey of the Nojima fault ruptured in the
 581 1995 Kobe earthquake, southwest Japan, *J. Geophys. Res.*, 105(B7), 16161–16171,
 582 doi:10.1029/2000JB900086.

583 Ozawa, K., and S. Takizawa (2007), Amorphous material formed by the mechanochemical effect in
 584 natural pseudotachylyte of crushing origin: A case study of the Iida-Matsukawa Fault,
 585 Nagano Prefecture, Central Japan, *J. Struct. Geol.*, 29(11), 1855–1869,
 586 doi:10.1016/j.jsg.2007.08.008.

587 Reches, Z. 'ev, and T. A. Dewers (2005), Gouge formation by dynamic pulverization during
 588 earthquake rupture, *Earth Planet. Sci. Lett.*, 235(1–2), 361–374,
 589 doi:10.1016/j.epsl.2005.04.009.

590 Remitti, F., S. A. F. Smith, S. Mittempergher, A. F. Gualtieri, and G. Di Toro (2015), Frictional
 591 properties of fault zone gouges from the J-FAST drilling project (Mw 9.0 2011 Tohoku-Oki
 592 earthquake), *Geophys. Res. Lett.*, 42(8), 2691–2699, doi:10.1002/2015GL063507.

593 Rempe, M., S. a. F. Smith, F. Ferri, T. M. Mitchell, and G. Di Toro (2014), Clast-cortex aggregates
 594 in experimental and natural calcite-bearing fault zones, *J. Struct. Geol.*, 68, 142–157,
 595 doi:10.1016/j.jsg.2014.09.007.

596 Sammis, C. G., and Y. Ben-Zion (2008), Mechanics of grain-size reduction in fault zones, *J.*
 597 *Geophys. Res.*, 113(B2), doi:10.1029/2006JB004892.

598 Schleicher, A. M., B. A. Van der Pluijm, and L. N. Warr (2010), Nanocoatings of clay and creep of
 599 the San Andreas fault at Parkfield, California, *Geology*, 38(7), 667–670,
 600 doi:10.1130/G31091.1.

601 Smith, S. A. F., S. Nielsen, and G. Di Toro (2015), Strain localization and the onset of dynamic
 602 weakening in calcite fault gouge, *Earth Planet. Sci. Lett.*, *413*, 25–36,
 603 doi:10.1016/j.epsl.2014.12.043.

604 Spagnuolo, E., O. Plümper, M. Violay, A. Cavallo, and G. Di Toro (2015), Fast-moving
 605 dislocations trigger flash weakening in carbonate-bearing faults during earthquakes, *Sci.*
 606 *Rep.*, *5*, 16112, doi:10.1038/srep16112.

607 Tinti, E., P. Spudich, and M. Cocco (2005), Earthquake fracture energy inferred from kinematic
 608 rupture models on extended faults, *J. Geophys. Res. Solid Earth*, *110*(B12), B12303,
 609 doi:10.1029/2005JB003644.

610 Ufer, K., G. Roth, R. Kleeberg, H. Stanjek, R. Dohrmann, and J. J. Bergmann (2004), Description
 611 of X-ray powder pattern of turbostratically disordered layer structures with a Rietveld
 612 compatible approach, *Z. Für Krist.*, *219*(9), 519–527, doi:10.1524/zkri.219.9.519.44039.

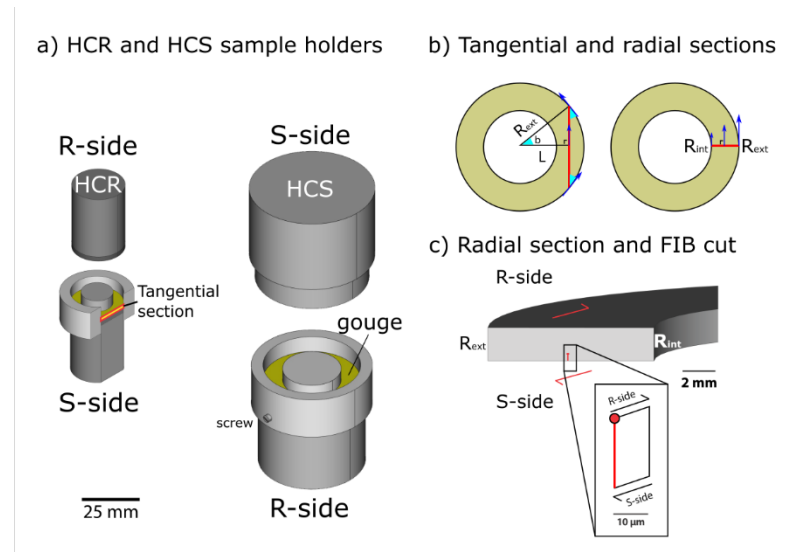
613 Verberne, B. A., O. Plümper, D. M. de Winter, and C. J. Spiers (2014), Superplastic nanofibrous
 614 slip zones control seismogenic fault friction, *Science*, *346*(6215), 1342–1344,
 615 doi:10.1126/science.1259003.

616 Veveakis, E., I. Vardoulakis, and G. Di Toro (2007), Thermoporomechanics of creeping landslides:
 617 The 1963 Vaiont slide, northern Italy, *J. Geophys. Res.*, *112*(F3),
 618 doi:10.1029/2006JF000702.

619 Westphal, T., T. Füllmann, and H. Pöllmann (2009), Rietveld quantification of amorphous portions
 620 with an internal standard—Mathematical consequences of the experimental approach,
 621 *Powder Diffr.*, *24*(3), 239–243, doi:10.1154/1.3187828.

622 Yund, R. A., M. L. Blanpied, T. E. Tullis, and J. D. Weeks (1990), Amorphous material in high
 623 strain experimental fault gouges, *J. Geophys. Res. Solid Earth*, *95*(B10), 15589–15602,
 624 doi:10.1029/JB095iB10p15589.

625 **Figures and Tables captions**



626

627 **Figure 1.** a) The sample assemblage of the experiments performed with ROSA (HCR) and
628 SHIVA (HCS) comprised a couple of hollow stainless steel specimen holders (medium gray) with,
629 respectively, 7.5/12.5 and 15/25 mm inner/outer radii (R_{int}/R_{ext}). To confine the gouge (yellow) two
630 Teflon parts (light grey) were used: a cylinder inserted in the inner hole and a ring positioned
631 externally. The outer ring was cut at ca. 60° to its basal surface and tightened to the metal gouge
632 holders with a stainless steel hose clamp. In the SHIVA experiments the Teflon components were
633 fixed with screws to the specimen metal holder. The red cross-sections represent the tangential
634 section on HCR (Figure 1b). b) Tangential and radial sections geometry. The tangential section is
635 cut at distance from the axis $L=0.5 \cdot (R_{int}+R_{ext})$. Because of this, from the center to the edge of the
636 section, radius varies as $R_{ext} \leq r \leq L$ and b , the angle between the section and the slip vector (blue
637 arrows), varies as $0^\circ \leq b \leq 37^\circ$ (according to $b=\arccos(L/R_{ext})$). In the radial section geometry, radius r
638 varies as $R_{int} \leq r \leq R_{ext}$ and angle b is always 90° . c) Orientation of the FIB cut. The FIB cut is
639 orthogonal to the radial section, therefore is parallel to the slip vector, with shear sense as indicated.

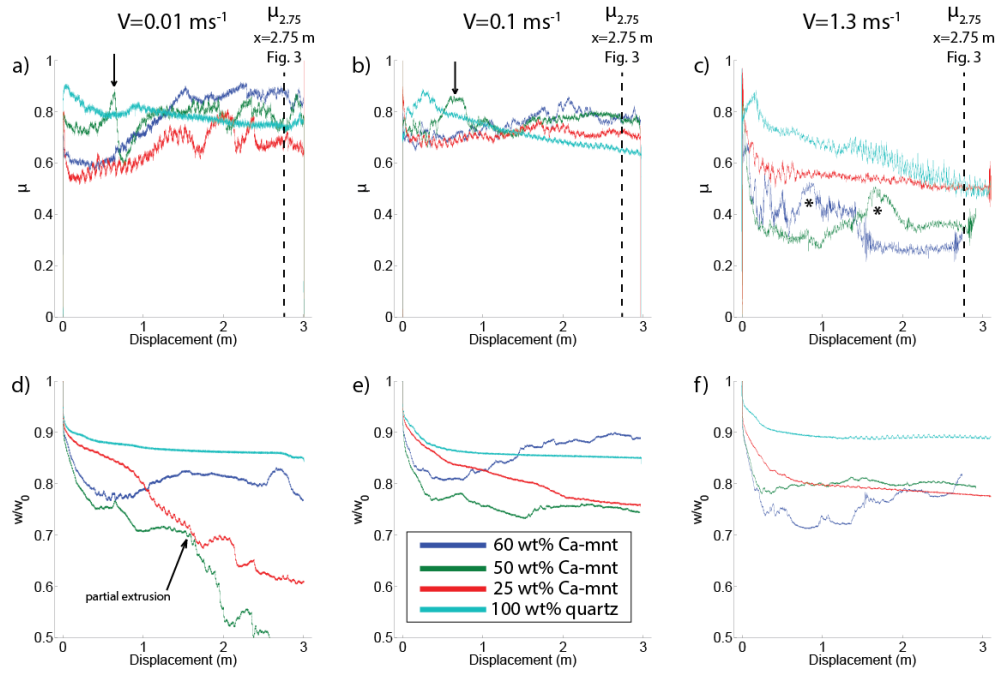


Figure 2. Friction coefficient μ (a to c) and normalized thickness w/w_0 (d to f) versus displacement for experiments performed at $V=0.01, 0.1$ and 1.3 ms^{-1} in ROSA. The black dashed lines mark the position for the averaged value $\mu_{2.75}$ (see Figure 3, Supplementary Table 1). Black arrows in a) and b) mark the second peak in friction coefficient observed in 50 wt.% Ca-mnt experiments at $V \leq 0.1 \text{ ms}^{-1}$; the arrow in d) marks the onset of gouge extrusion for 25 and 50 wt.% Ca-mnt experiments at $V = 0.01 \text{ ms}^{-1}$. Stars in c) mark large variations in friction coefficient (60 and 50 wt.% Ca-mnt experiments at 1.3 ms^{-1}).

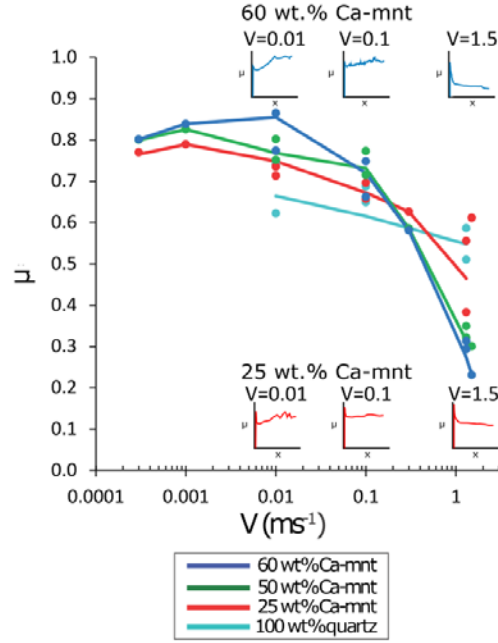


Figure 3. Friction coefficient averaged between 2.725-2.775 m displacement ($\mu_{2.75}$) versus slip rate. Colored lines interpolate $\mu_{2.75}$ at increasing slip rate for different Ca-mnt content. Insets report for reference the evolution of μ with displacement for 60 wt.% (blue line) and 25 wt.% (red line) Ca-mnt.

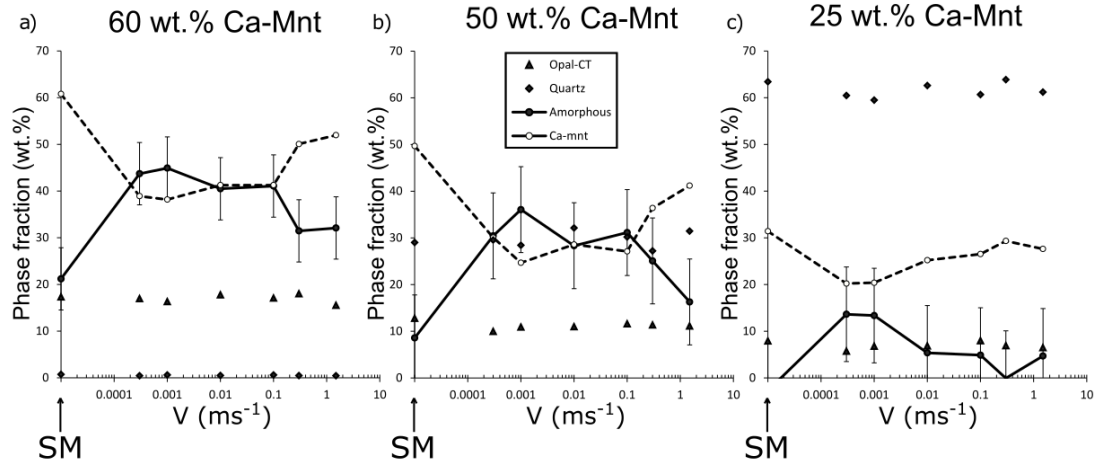
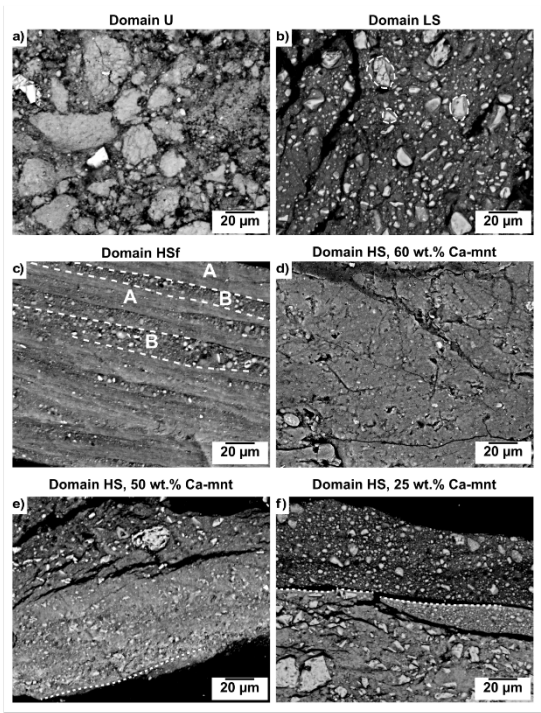


Figure 4. Quantitative phase analysis results (Section 3.2 and Table 1). Phase content is plotted versus slip rate (arrows indicate the undeformed materials), for each composition: a), b) and c) for 60, 50 and 25 wt.% Ca-mnt, respectively. Error bars show the accuracy of the amorphous phase estimate calculated after [Westphal *et al.*, 2009] (Section 2.3, Table 1). Opal and quartz wt.%

658 are independent of the imposed slip rate. Instead, for all tested initial gouge mixtures, the amount of
 659 amorphous material increases at the expense of Ca-mnt with decreasing slip rate.



660
 661 **Figure 5.** Backscattered SEM images of the microstructural domains. a) domain U (60 wt.%
 662 Ca-Mnt) contains angular quartz clasts and sub-rounded aggregates of opal and Ca-mnt (grain size
 663 <100 µm); b) domain LS (60 wt.% Ca-Mnt), characterized by sub-rounded opal and quartz clasts
 664 (grain size <20-50 µm). Clasts form CCAs and are surrounded by a Ca-mnt-rich matrix; c) domain
 665 HSf (60 wt.% Ca-Mnt), with dashed lines delimiting subdomains A and B. A has a foliated, sub-
 666 micrometric texture. B has abundant CCAs (<2 µm) in a sub-micrometric matrix. d) Domain HS
 667 (60 wt.% Ca-mnt) has a sub-micrometric texture, similar to A, but with no foliation. e) Domain HS
 668 (50 wt.% Ca-mnt) is similar to d), despite a higher abundance of quartz in the sub-micrometric
 669 matrix and occurrence of occasional wavy Y-shears (white dashed line). f) Domain HS (25 wt.%
 670 Ca-mnt) has abundant sub-rounded quartz and opal grains (0.1-5 µm) in a Ca-mnt matrix, crosscut
 671 or delimited by wavy Y-shears (white dashed line).

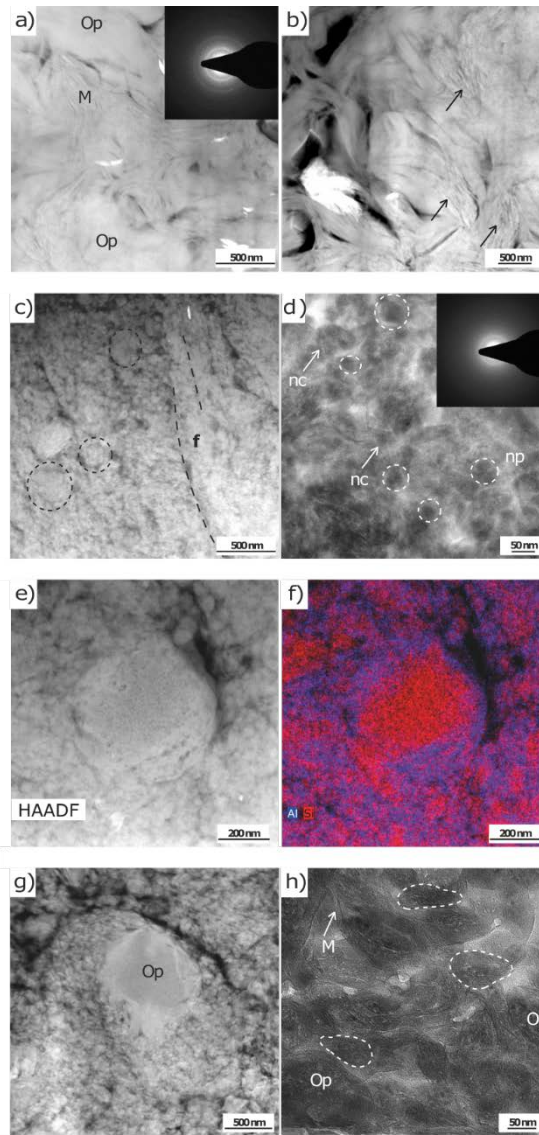
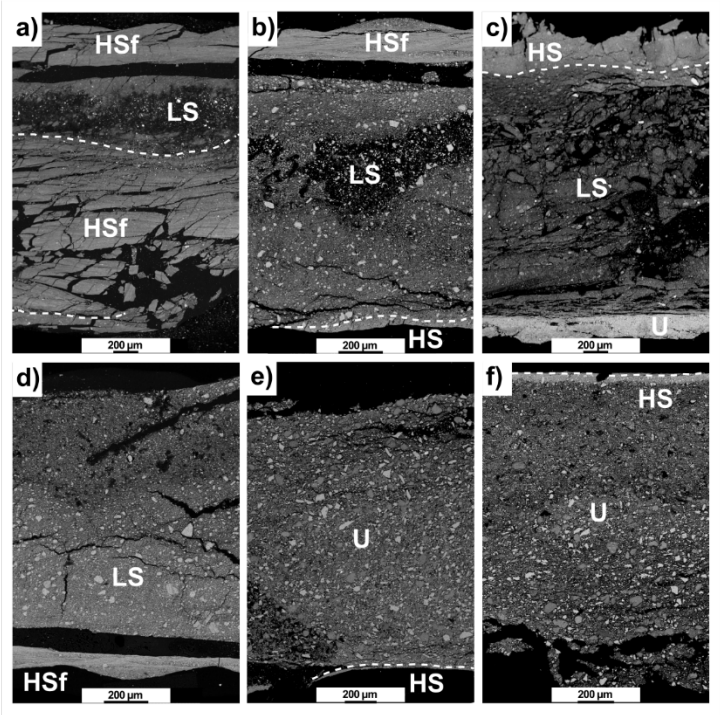


Figure 6. TEM images of the microstructural domains. a) Domain U: Ca-mnt (M) and Opal (Op) at the nanoscale (HAADF image); SAED subset shows Ca-mnt diffraction rings. b) Domain U at higher magnifications: in some areas (black arrow), Ca-mnt and opal are interlayered (HAADF image). c) Domain HSf: rounded clusters of nanoparticles, <200 nm grain size (black dashed circles), are widespread (HAADF image). Nano-foliations appear like densely packed nanoparticles in fiber-shaped clusters, ca. 100 nm thick ("f", black dashed lines). d) Domain HSf at higher magnifications: nanoparticles with grain size of 10-50 nm ("np", white dashed lines) and Ca-mnt nanocrystals having grain size of ca. 50x5 nm ("nc", white arrows) (BF image); SAED diffraction pattern showing diffuse scattering from nanoparticles and diffraction rings from nanocrystals. e) CCA within domain HSf, grain size < 500 nm, having opal or quartz core and nanoparticles cortex

684 (HAADF image); f) TEM-EDS chemical map of the CCA in e): the nanoparticles of the cortex have
685 a Ca-mnt composition (purple). In the CCA cortex and in the nanoparticles matrix occasionally Si-
686 rich areas (red) may be due to the occurrence of smaller opal grains (Al=blue, Si=red). g) Domain
687 HS: CCA, grain size ca. 700 nm, with opal core and nanoparticles in the cortex, surrounded by a
688 nanoparticle-rich matrix (HAADF image). h) Domain HS at higher magnifications: nanoparticles
689 have an internal organization as nano-CCAs (white dashed contour), with opal cores rimmed by Ca-
690 Mnt nanocrystals. Nanocrystals with a visible lattice periodicity are widespread in the matrix
691 between the nano-CCAs (BF image).



692
693 **Figure 7.** Backscattered SEM images of the sheared gouge layers. Slipping zones from Ca-
694 mnt ≥ 50 wt.% (a to c) and Ca-mnt=25 wt.% (d to f) starting material, deformed at $V=0.001 \text{ ms}^{-1}$,
695 $V=0.1 \text{ ms}^{-1}$ and $V=1.3 \text{ ms}^{-1}$, respectively. The distribution of the microstructural domains is
696 dependent on both initial composition and imposed slip rate (see Figure 8). The white dashed lines
697 mark the boundaries between microstructural domains.

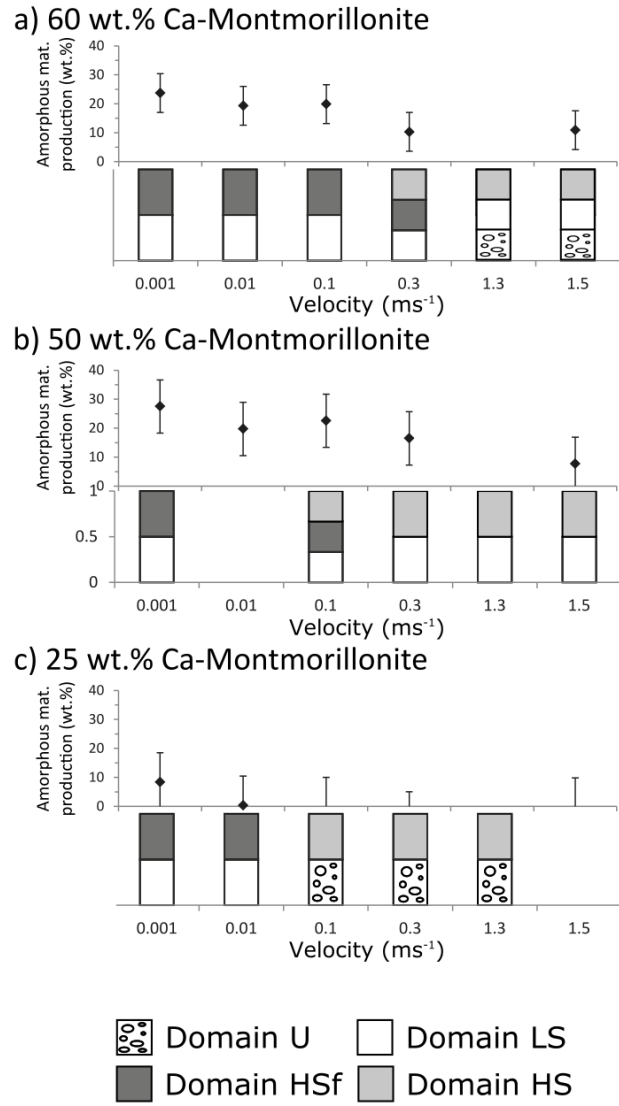


Figure 8. Occurrence of the microstructural domains and amorphous material production (i.e. amorphous material after the experiment minus amorphous material in the starting material) with respect to the composition of the starting materials and slip rate. a) to c) Ca-mnt content of 60, 50 and 25 wt.% in the starting material. Domain U was found in experiments performed at $V \geq 1.3$ ms⁻¹ (60 wt.% Ca-mnt) and at $V \geq 0.1$ ms⁻¹ (25 wt.% Ca-mnt). Domain LS was found in all the experiments except those performed at $V \geq 0.1$ ms⁻¹ (25 wt.% Ca-mnt). Domain HSf was found in the gouges sheared at $V \leq 0.1$ ms⁻¹ (Ca-mnt ≥ 50 wt.%), and at $V \leq 0.01$ ms⁻¹ (25 wt.% Ca-mnt). Domain HS was found at $V \geq 0.3$ ms⁻¹ in 60 wt.% Ca-mnt and at $V \geq 0.1$ ms⁻¹ in 50 and 25 wt.% Ca-mnt

gouges. The largest production of amorphous materials (25-28 wt.%) occurs for Ca-mnt \geq 50%, low slip rates and in the presence of domain HSf.

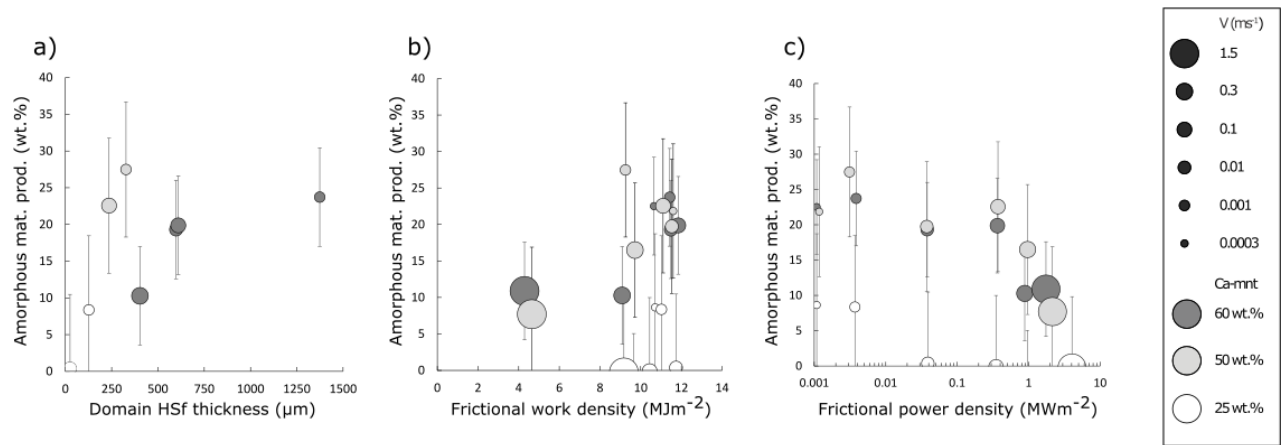


Figure 9. Amorphous material production (i.e. amorphous material after the experiment

minus amorphous material in the starting material) as function of domain HSf thickness, frictional work density (FWD) and frictional power density (FPD). Error bars indicate the uncertainty in the amorphous material content estimate (see also Figure 4, Section 3.2 and Table 1). The radius of the symbols is proportional to the imposed slip rate in the experiment; the grey scale is related to the starting material composition. a) The production of amorphous material is proportional to the thickness of domain HSf, the Ca-mnt content in the starting material and to the decrease of the imposed slip rate. b) For all gouge mixtures, the amorphous production is positively correlated with frictional work density (FWD). The highest increase occurs for $V \leq 0.1$ ms⁻¹. c) The amorphous material production is inversely correlated with frictional power density (FPD) and thus with the slip rate of the experiment.

| Table 1. Resume of the Rietveld quantitative phase analysis | | | | | | | | | | |
|--|------------------|--------|--------|---------|--------|-------|--------|---------|--------|--------|
| exp | V | Ca-mnt | er. | Opal-CT | er. | Qtz | er. | Amorph. | er. | acc. |
| # | ms ⁻¹ | wt. % | ±wt. % | wt. % | ±wt. % | wt. % | ±wt. % | wt. % | ±wt. % | ±wt. % |
| 60 wt% Ca-mnt | | | | | | | | | | |
| S.M. | - | 60,8 | 0,3 | 17,3 | 0,3 | 0,7 | 0,1 | 21,2 | 0,6 | 6,7 |
| 218 | 0,0003 | 38,9 | 0,5 | 16,9 | 0,5 | 0,4 | 0,1 | 43,7 | 1,1 | 6,7 |
| 210 | 0,001 | 38,2 | 0,5 | 16,3 | 0,5 | 0,6 | 0,1 | 44,9 | 1,0 | 6,7 |
| 274 | 0,01 | 41,3 | 0,5 | 17,8 | 0,5 | 0,5 | 0,1 | 40,5 | 1,1 | 6,7 |
| 216 | 0,1 | 41,3 | 0,5 | 17,1 | 0,5 | 0,6 | 0,0 | 41,1 | 1,0 | 6,7 |
| 217 | 0,3 | 50,1 | 0,5 | 18,0 | 0,4 | 0,5 | 0,1 | 31,5 | 0,9 | 6,7 |
| 238 | 1,5 | 52,0 | 0,5 | 15,5 | 0,5 | 0,4 | 0,1 | 32,1 | 1,0 | 6,7 |
| 50 wt% Ca-mnt | | | | | | | | | | |
| S.M. | - | 49,7 | 0,4 | 12,8 | 0,3 | 29,0 | 0,3 | 8,6 | 1,0 | 9,2 |
| 280 | 0,0003 | 30,1 | 0,5 | 10,0 | 0,2 | 29,5 | 0,3 | 30,4 | 1,0 | 9,2 |
| 245 | 0,001 | 24,7 | 0,6 | 10,9 | 0,3 | 28,4 | 0,3 | 36,1 | 1,2 | 9,2 |
| 243 | 0,01 | 28,6 | 0,6 | 11,0 | 0,3 | 32,1 | 0,4 | 28,3 | 1,2 | 9,2 |
| 229 | 0,1 | 27,1 | 0,5 | 11,6 | 0,3 | 30,2 | 0,3 | 31,1 | 1,1 | 9,2 |
| 242 | 0,3 | 36,4 | 0,5 | 11,3 | 0,3 | 27,2 | 0,3 | 25,1 | 1,0 | 9,2 |
| 228 | 1,5 | 41,2 | 0,6 | 11,1 | 0,3 | 31,5 | 0,4 | 16,3 | 1,2 | 9,2 |
| 25 wt% Ca-mnt | | | | | | | | | | |
| S.M. | - | 31,4 | 0,5 | 7,9 | 0,3 | 63,4 | 0,4 | -2,7 | 1,3 | 10,1 |
| 279 | 0,0003 | 20,2 | 0,7 | 5,7 | 0,3 | 60,4 | 0,5 | 13,6 | 1,5 | 10,1 |
| 281 | 0,001 | 20,4 | 0,6 | 6,8 | 0,3 | 59,5 | 0,5 | 13,4 | 1,4 | 10,1 |
| 266 | 0,01 | 25,2 | 0,6 | 6,8 | 0,3 | 62,6 | 0,5 | 5,4 | 1,4 | 10,1 |
| 276 | 0,1 | 26,5 | 0,6 | 7,9 | 0,3 | 60,7 | 0,4 | 4,9 | 1,3 | 10,1 |
| 271 | 0,3 | 29,3 | 0,6 | 6,9 | 0,4 | 63,8 | 0,5 | -0,1 | 1,5 | 10,1 |
| 268 | 1,5 | 27,6 | 0,6 | 6,5 | 0,3 | 61,2 | 0,4 | 4,7 | 1,3 | 10,1 |

Table 1. Results of the quantitative XRPD phase analysis. Exp = number of the experiment
V (ms⁻¹) = slip rate; Ca-mnt, Opal-CT, Qtz (wt.%) = Ca-Montmorillonite, Opal-CT and Quartz with
err. (wt.%) = error of Rietveld refinement technique; Amorph. (wt.%) = amorphous material content
and err. (wt.%) = sum of the errors for each phase; Acc. (wt.%) = accuracy of amorphous material
content estimation (Section 3.2).